



# Coaxial color channel focus evaluation to estimate standoff height in directed energy deposition additive manufacturing

Callan Herberger<sup>1</sup> · Lauren Heinrich<sup>2</sup> · Erik LaNeave<sup>1</sup> · Brian Post<sup>2</sup> · Kenton B. Fillingim<sup>2</sup> · Eric MacDonald<sup>1,2</sup> · Thomas Feldhausen<sup>2</sup> · James Haley<sup>2</sup>

Received: 16 April 2023 / Accepted: 19 January 2024  
© Springer Nature Switzerland AG 2024

## Abstract

Directed energy deposition (DED) is an additive manufacturing process that is being rapidly adopted by industry and is well suited for the fabrication of complex components in a variety of metal alloys. In laser cladding systems such as DED, powder is blown in a stream to a metal substrate coincident with a laser necessary to deposit molten metal with 3D spatial control. The focus of both the laser and the powder stream are crucial, and best deposition occurs at a predetermined standoff height between the build surface and the print head. Generally, no monitoring of this distance is implemented in commercial DED systems. Due to potential over or under building, the standoff height often changes over time but tends to self-correct. However, inexpensive and minimally intrusive methods to identify optimal standoff are required to provide real-time control to maintain the optimal distance. The present work explores the quantification of the focus of the three-color channels of a coaxial camera to determine the standoff height. An experiment was performed in which a 254 mm wall is built and the standoff height, initially 5.0 mm below the optimal position, was then intentionally increased every 25.4 mm of wall length by an amount of 1.0 mm to a final position 7.0 mm above optimal. Computer vision is demonstrated to monitor the amount of focus in each color band and estimate standoff distance. A response can be calculated in under 40 ms using simple hardware and can work in most laser-based DED systems.

**Keywords** Hybrid directed energy deposition · Standoff height · Computer vision · Focus quantification

## 1 Introduction

Advanced manufacturing is transforming with the new digital paradigm of additive manufacturing (AM) with benefits, including design freedom and mass customization [1–4], reduced material waste, and decreased buy-to-fly ratios [5–8]. The billet feedstock used in machining can be prohibitively expensive and AM can more efficiently deposit material only where necessary. Complex geometries fabricated by directed energy deposition improve performance and efficiency of aerospace parts and other industrially relevant applications like tooling and light-yet-sufficiently-strong lattices [9]. Furthermore, the composition of the final metal

structure can be modulated compositionally with the simultaneous use of different metal powder in changing ratios for functionally graded structures [10–12], as well as with embedded components [13, 14] to improve performance and embed additional functionalities in otherwise load-bearing structures.

One critical deposition parameter that is determined by the manufacturer is the standoff height, which is defined in this evaluation as the distance between the bottom of the deposition nozzle and the top of the previously deposited layer. At the ideal distance, the coaxial laser focal diameter as well as the powder focal distance converge with optimal catchment efficiency and desired energy density [15]. When this distance decreases during an overbuilding condition, indicating that the actual deposited layer height was greater than the programmed layer height, a decrease in powder catchment efficiency occurs as well as an increase in energy density, where more thermal laser energy is added per volume mass deposited than expected. During this condition, the actual deposited layer height begins to decrease

✉ Callan Herberger  
caherberger@miners.utep.edu

<sup>1</sup> The University of Texas at El Paso, El Paso, TX 79968, USA

<sup>2</sup> Manufacturing Science Division, Oak Ridge National Laboratory, Oak Ridge, TN 37831, USA

to the programmed layer height due to the decreased powder catchment as the distance from the powder convergence zone decreases. On the contrary, during an underbuilding condition where the deposited layer height is less than the programmed layer height, a diverging condition occurs if no deposition parameters are changed. The laser spot diameter diverges as well as the intersecting powder streams delivering the feedstock creating constantly decreasing powder catchment efficiency condition. Even with this tendency to self-correct in overbuilding, a variation is introduced in the layer thicknesses across the build. Consequently, a real-time estimation of the standoff is necessary to provide feedback to control the standoff and provide optimal deposition throughout the build. In an underbuilding case with no tendency to self-correct, standoff-height estimation is critical.

Computer vision is one process monitoring approach to better control standoff distance through applied weld pool imaging. Weld pool images are commonly captured with low spatial and spectral resolution sensors—capable of identifying irregularities in DED structures [16, 17]. Extraction of weld pool geometry through computer vision allows for the control of machine parameters [18, 19] and identification of microstructure defects [20]. Melt pool characteristics can be used to identify the effect of adjusting process parameters [21–24]. These methods track melt pool geometry and optimize machine parameters, maintaining melt pool features within the desired range. Higher spectral resolution and infrared sensors are able to extract true dimension features of the melt pool to leverage variation between the solid–liquid transitions [25–27]. Instabilities can be identified when melt pool images are processed with neural networks [20, 28]. These optical features have been evaluated by machine learning, and Deep Convolutional Neural Networks have outperformed traditional segmentation for in-situ per pixel classification of weld pool and spatter [29]. Coaxial weld pool imaging is a popular method for characterizing thermal history which can be complex depending on the target geometry [30], identifying locations of porosity [31], and identifying porosity formation through the monitoring of melt pool and powder interactions [32, 33].

Autofocus measurement calculates a metric to encode the amount of high-frequency information in an image to optimize the focal length of a zoom lens. High frequencies are correlated to the sharp edges of an in-focus image [34–36]. Focus measurement algorithms [37–39] have been leveraged to calculate focus values globally for each spectral band separately. In this work, we present a non-obtrusive method to leverage focal length variations between color channels which enable the standoff between the nozzle and weld pool to be estimated based on the focus value of each channel.

Machine variables, like laser power, traverse feed, and powder feed rate, can accelerate part growth causing deviation from defined layer height. Deposition rate is strongly influenced by laser and powder overlap. Haley et al. used an analytical model to show how working distance convergence is dependent on many interactions, including laser attenuation, melt pool geometry, and powder dispersion [15]. Modulating parameters to keep weld pool features consistent without consideration of standoff height can have unintended secondary consequences on the final material properties and part geometry [40]. For these reasons, standoff needs to be calculated in-situ for consistent updating to layer height command [41]. Monitoring working distance has been approached with multiple methodologies, including off-axis camera setups [42–46], 3D scanners [47, 48], and laser triangulation [46, 49–51]. Hardware to measure standoff height requires installation inside or near the build chamber where occlusions and part geometry can limit measurement accuracy as well as cause potential head collisions. Leveraging differences in reflected spectral intensities through laser optics to calculate standoff in laser welding and direct casting was used to eliminate the need for specialized hardware [52]. Image classification has shown the possibility to identify standoff height from monochromatic weld pool images taken coaxially [53]. The use of coaxial imaging has the advantage of having unobscured views during the entire build and does not need space within the build chamber for equipment.

The present work advances the field of computer vision in directed energy deposition by capturing coaxial weld pool images using a prism RGB sensor in which chromatic aberrations between spectral bands result in focal length differences with maximum focus at different standoff heights for each RGB channel. The known distance between peak focus for each channel allows for robust calculation of standoff height. Red, green, and blue focus measurements were then combined to obtain a feedback control signal. This signal could be leveraged to optimize the process in real time by adjusting either the distance of the head to the build layer or the speed of the build head to modulate the deposition, impacting the next layer thickness in the order of milliseconds based on each coaxial image.

## 2 Materials and methods

A directed energy deposition system was used to create a 254 mm wall with intentional inserted error in the standoff height. Computer vision was used to identify image features that could be correlated to the intentionally varying distance.

155 **2.1 Directed energy deposition system**

156 A hybrid Okuma MU-8000V Laser EX with a Trumpf  
 157 additive system was used to manufacture the components  
 158 evaluated in this experiment. The system is equipped with a  
 159 Trumpf TruDisk 4002 infrared laser as well as a nozzle with  
 160 three discrete powder delivery ports and 12 mm standoff  
 161 that can process using a 0.6–6.0 mm programmed laser spot  
 162 size. 316L stainless steel was utilized as the substrate and  
 163 the deposited feedstock was MetcoAdd 316L stainless steel  
 164 powder with a particle range of  $-105 + 45 \mu\text{m}$  at a flow rate  
 165 of 12 g/min. A programmed spot size of 3.5 mm was used  
 166 at a laser power of 2 kW and a traverse rate of 900 mm/min.  
 167 This system can be seen in Fig. 1.

168 **2.2 Tool path generation of varying height**  
 169 **deposition experiment**

170 The Okuma MU-8000V Laser EX was used to produce  
 171 a single bead vertical wall using blown powder DED.  
 172 The wall was 254 mm long with ten 25.4 mm-long sections.  
 173 Each segment of the wall was printed at varying  
 174 standoff height between a range of 7 mm and 16 mm, with  
 175 12 mm as the manufacturer’s recommended working distance  
 176 for optimal powder capture. Starting at 7 mm stand-  
 177 off height, the Okuma would print one 25.4 mm section  
 178 before increasing standoff height by 1 mm. This program  
 179 was continued until manually stopped after 12 layers were  
 180 consecutively built. Figure 2a shows a schematic of the  
 181 build plan which intentionally changes the Z height of the  
 182 deposition head to non-optimal values and the deposition

Fig. 1 Hybrid blown powder DED system used for coaxial imaging

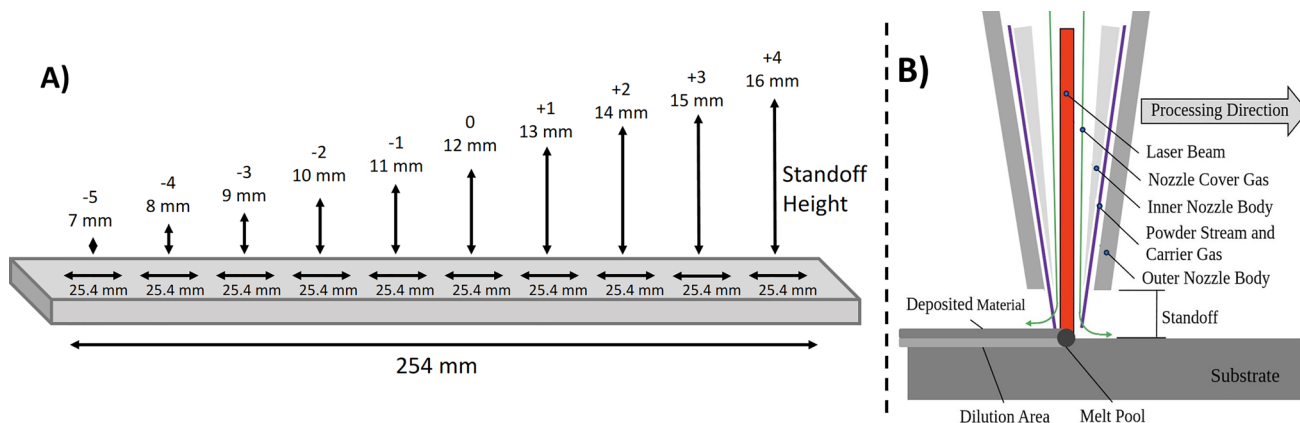
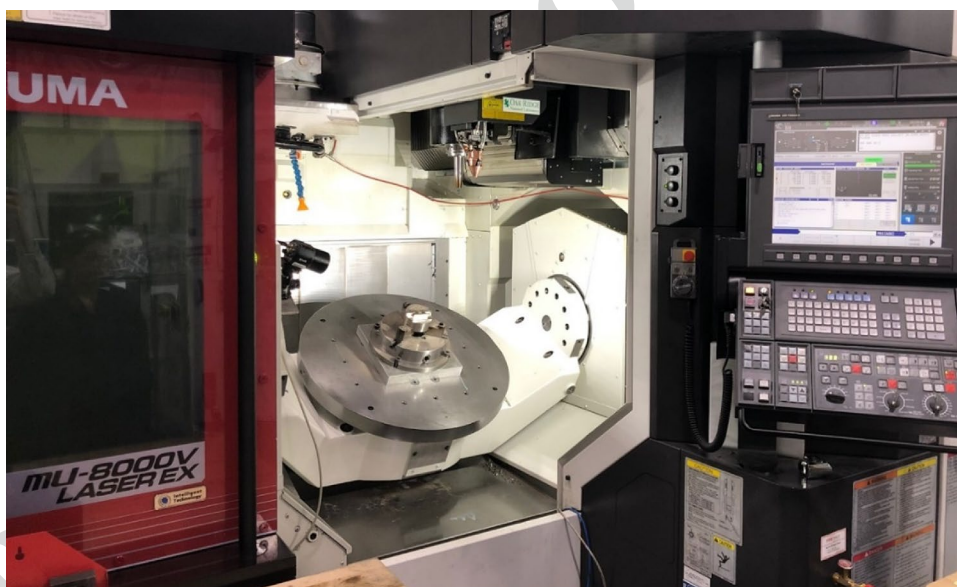


Fig. 2 a Tool path to fabricate a 254 mm wall with increased 1 mm standoff height after each 25.4 mm of travel. b Blown powder DED process schematic

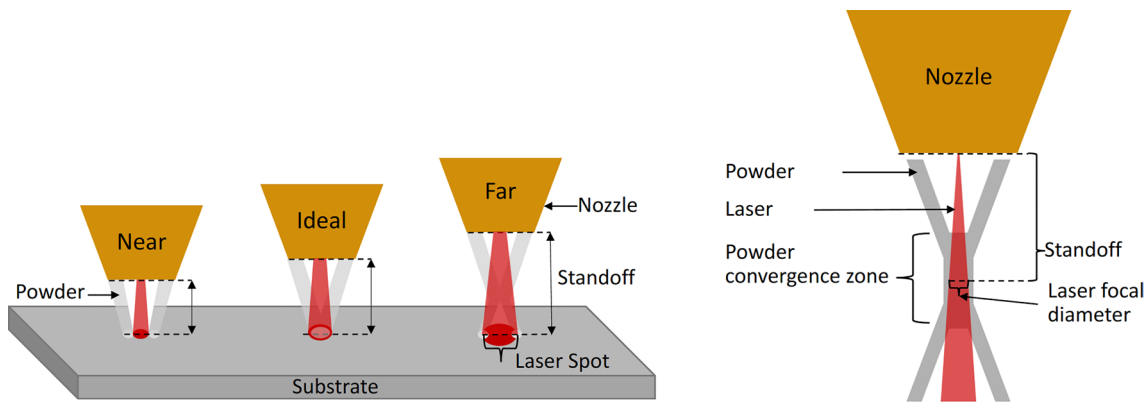


Fig. 3 Effect of standoff height on laser and powder spot size

183 process. Figure 2b shows a schematic explaining the blown  
 184 powder build head. Figure 3 illustrates how when the laser  
 185 and powder beams are not at the optimal height, a detri-  
 186 mental defocusing occurs which reduces the efficiency of  
 187 the deposition.

188 **2.3 Coaxial imaging of laser cladding deposition**

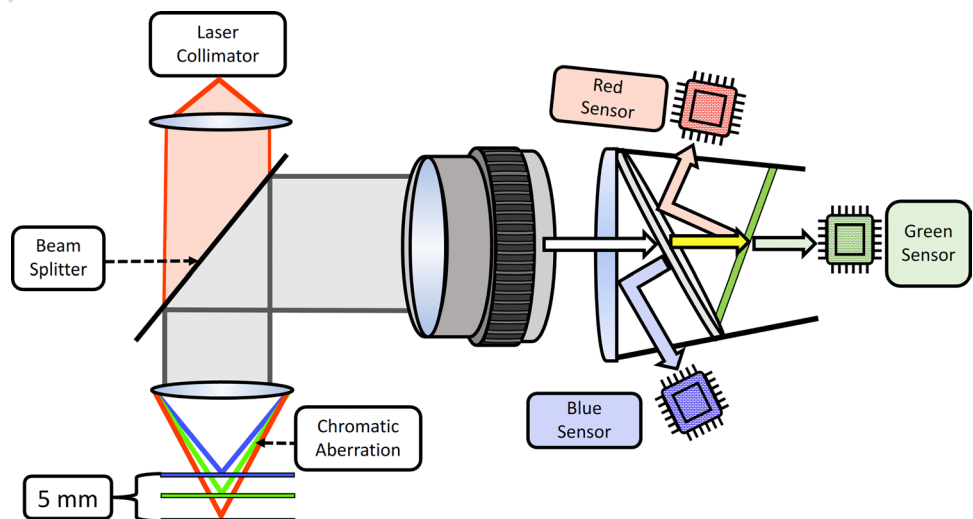
189 A JAI Apex AP-3200T-USB camera was used to capture  
 190 the coaxial color images during the deposition process at  
 191 a rate of 20 Hz. The coaxial camera views the melt pool  
 192 through the same focal optics used for the laser with a  
 193 dichroic beam splitter. Chromatic dispersion is created by  
 194 the primary laser focal optics Fig. 4 (left). The coaxial  
 195 camera utilizes a prism camera sensor depicted in Fig. 4  
 196 (right). A prism sensor has a better spectral response,  
 197 Fig. 5, which along with the different RGB focal lengths  
 198 can be leveraged to extract depth information from fre-  
 199 quency content of each band. When the melt pool is at the  
 200 nominal working distance, the green channel is in focus.

Due to chromatic aberration of the objective lens opti- 201  
 mized for the NIR laser, the blue and red focal planes 202  
 are slightly above and below the nominal working dis- 203  
 tance. This limits the range in which the standoff height 204  
 can be effectively estimated, as outside of the individual 205  
 RGB channel’s focus range, images can no longer be differ- 206  
 entiated. The discovered range of this optical setup pro- 207  
 duced a range of  $\pm 2.5$  mm from optimal standoff height. 208  
 209

**2.4 Computer vision techniques to identify optimal 210  
 standoff height 211**

Raw coaxial weld pool images were masked to isolate the 212  
 weld pool and remove internal reflections from within the 213  
 nozzle. A small Gaussian blur was applied to reduce optic 214  
 and sensor noise. Sensor noise introduces pixel intensity 215  
 changes that can be misidentified as high-frequency focus 216  
 information. Finally, color images were split into separate 217  
 grayscale images for each RGB band. To extract a focus 218  
 measurement (FM) value for the three separate RGB

Fig. 4 Chromatic aberration effect from laser focal optics (left) and internal structure of prism-based camera sensor (right)



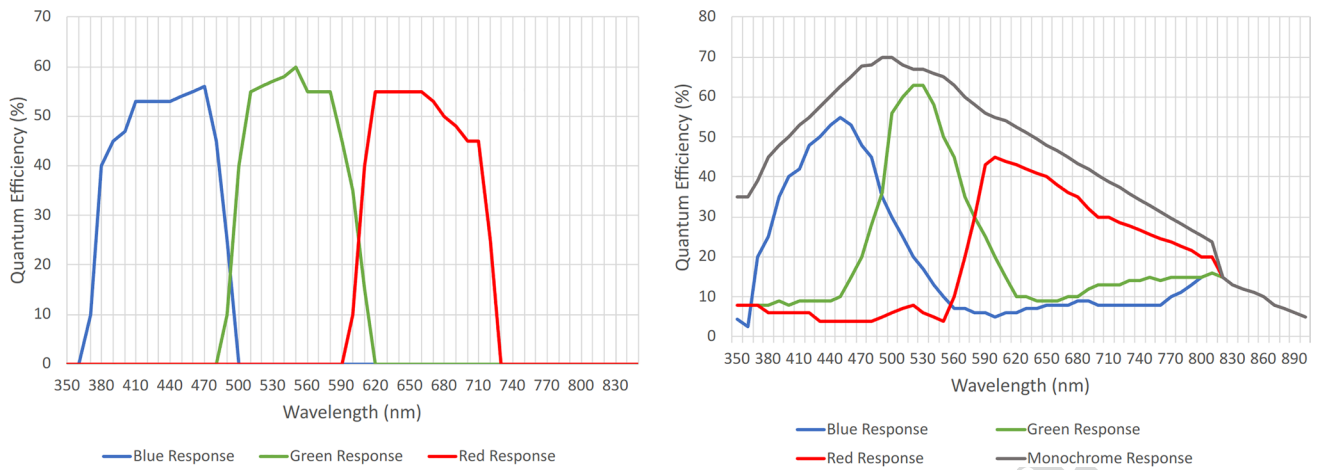


Fig. 5 Comparison of the spectral responses between a Prism (left) and Bayer camera sensor (right)

bands, each grayscale image was processed with focus measurement algorithms. 28 FM algorithms were tested in total and compared. The primary criterion was the algorithm's ability to precisely detect the in-focus state of the weld pool. Additional factors considered comprise unimodality, a sharp signal response, and computation speed. Unimodality is crucial for determining peak focal measurement, while a sharp response is advantageous when combining into a unitless feedback control signal. For visual clarity, we narrowed down the comparison to five out of the 28 FM algorithms. Specifically, three of these algorithms demonstrated accuracy in identifying weld pool focus information, while the remaining two were unable to differentiate any focus information across images. The algorithms below are compared to illustrate the selection process.

### 2.4.1 Brenner's gradient

Difference between a pixel and its neighbor 2 away in horizontal and vertical directions

$$FM_{Brenner} = \sum_x \sum_y (i(x, y) - i(x + 2, y))^2 \quad (1)$$

### 2.4.2 Laplacian energy

Convolution of an image with the  $5 \times 5$  Laplace second derivative kernel  $\mathcal{L} = [10 - 20 1]$ . The final focus measurement is the sum of squares of the image pixel values after convolution.

$$FM_{LaplacianEnergy} = \sum_x \sum_y (i(x, y) * \mathcal{L})^2 \quad (2)$$

### 2.4.3 Modified Laplacian

An alternative definition to the Laplacian filter. The separable filter  $\mathcal{L}_x = [-1 - 2 - 1]$ ,  $\mathcal{L}_y = \mathcal{L}^T x$  is convolved with the image  $i(x, y)$ . Pixel summation then creates the final focus value

$$FM_{ModifiedLaplacian} = \sum_x \sum_y |i(x, y) * \mathcal{L}_x| + |i(x, y) * \mathcal{L}_y| \quad (3)$$

### 2.4.4 Tenengrad

A focus measure based on magnitude of the image gradients  $G_x$  and  $G_y$ , calculated by convolving with the Sobel operators

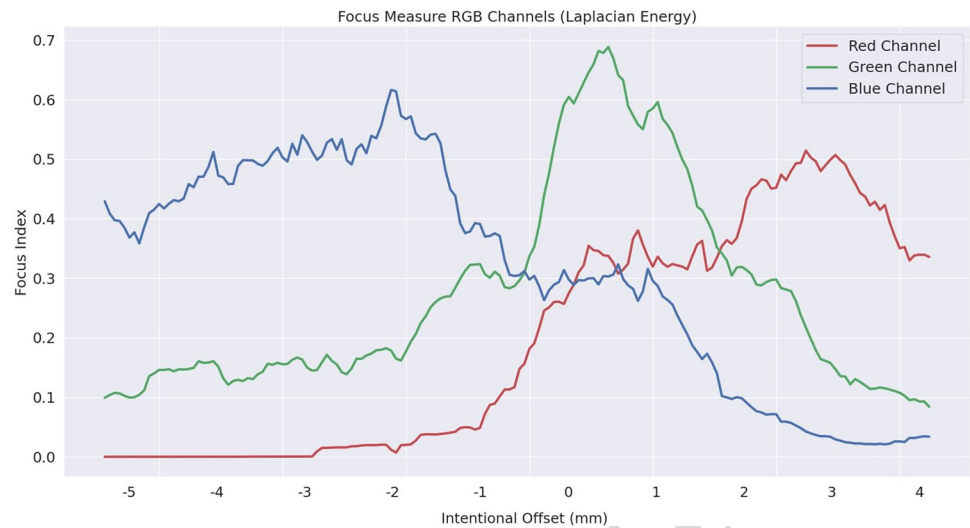
$$FM_{Tenengrad} = \sum_x \sum_y G_x(x, y)^2 + G_y(x, y)^2 \quad (4)$$

### 2.4.5 Gray-level variance

The difference between each pixel in the image and mean gray-level intensity value is computed

$$FM_{GrayLevelVariance} = \sum_x \sum_y |i(x, y) - \mu| \quad (5)$$

**Fig. 6** Normalized Laplacian energy focus response for each individual RGB band



266 After calculating focus values for each red, green, and  
 267 blue band for every image, each response is normalized  
 268 using sklearn min–max scaler to place the values between  
 269 [0,1] as seen in Fig. 6. Focus can vary between adjacent  
 270 images due to factors such as weld pool size, sensor noise,  
 271 and number of satellite objects. To reduce the impact of  
 272 abrupt weld pool changes, a 10-frame (0.5 s) moving aver-  
 273 age was used to smooth the final output. To count satel-  
 274 lite objects, the color image was converted to grayscale,  
 275 blurred, and thresholded. After the weld pool was removed,  
 276 the remaining particles were counted and the total area in  
 277 pixels was computed. It was hypothesized that spatter count  
 278 may also correlate to standoff height.

### 279 3 Results

280 Experiments were performed to identify the best-suited  
 281 focus estimation algorithm with consideration of both the  
 282 accuracy of the method and the duration of calculation with  
 283 a final aim to implement in real time to control the head  
 284 distance during fabrication.

#### 285 3.1 Selection of focus algorithm

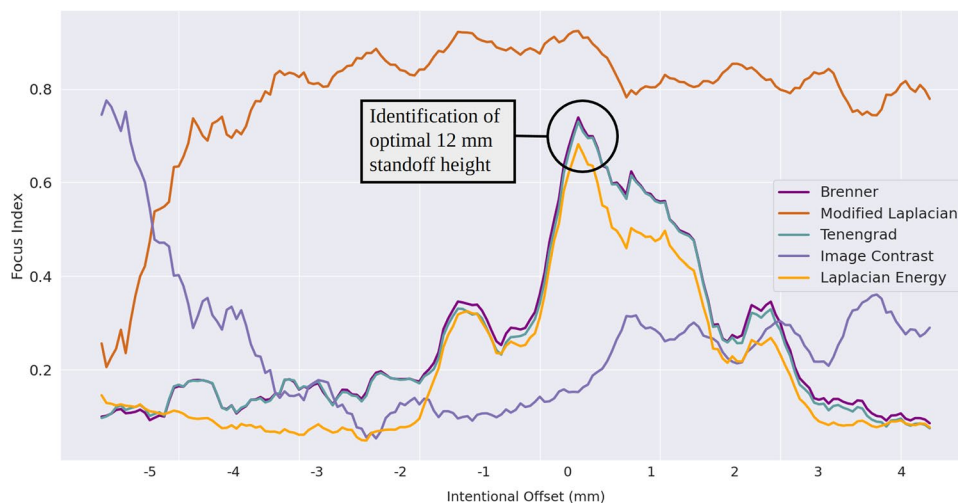
286 Focus measurement algorithms must identify the best  
 287 standoff height to be considered accurate. A unimodal  
 288 response is therefore required and must be centered  
 289 around an intentional offset of 0 mm. Other considerations  
 290 for effective real-time algorithms are the number of  
 291 computational operations and the speed of image analysis.  
 292 The most effective focus measurement performers were  
 293 Tenengrad, Brenner's, and Laplacian Energy with a  $5 \times 5$   
 294 kernel. These three focus measurement algorithms were  
 295 all accurate when identifying best standoff height and had

296 computational time quick enough for real-time control.  
 297 Of the 28 tested algorithms, there were only 8 that could  
 298 identify optimal standoff height and only the three discussed  
 299 here could be considered for in-situ analysis. Laplacian-  
 300 based focus operators need to perform convolution at  
 301 each pixel in the coaxial image with a Laplacian kernel.  
 302 Optimizations can be performed by transforming the  
 303 image to the Fourier domain (spatial frequency) and then  
 304 calculating a single multiplication with the Laplacian. The  
 305 Tenengrad algorithm requires performing two-directional  
 306 first derivatives, doubling the operations needed when  
 307 compared to Laplacian Energy. Brenner's focus operators  
 308 leverage high frequencies being highly dependent on  
 309 their spatial location. Shifting a copy of the image in both  
 310 the x- and y-direction and subtracting from the original  
 311 leaves strong edge information. Tenengrad, Brenner's,  
 312 and Laplacian energy are optimal focus measure operators  
 313 for in-situ standoff control. Computational speeds and  
 314 memory usage for five focus measurement algorithms are  
 315 compared in Table 1. Calculations were performed on an  
 316 Intel i7-9700k processor with no Graphics Processing Unit  
 317 (GPU) acceleration, Python 3.10, and NumPy 1.23.

**Table 1** Average computation time and memory usage

Focus measurement algorithm	Average image computation time (ms)	Memory usage (MiB)
Brenner	4.41	325.41
Laplacian energy	3.52	312.88
Modified Laplacian	6.95	308.77
Tenengrad	6.32	315.38
Gray-level variance	1.01	312.20

**Fig. 7** Comparison of green channel response among focus measurement algorithms



318 In terms of accuracy, Fig. 7 shows the performance of  
 319 each of the algorithms on the green channel of weld pool  
 320 images from layer one. The algorithm responds with a similar  
 321 shape for all RGB channels; green is selected to illustrate  
 322 the different algorithm’s ability to identify when the image is  
 323 in focus. Image Contrast and Modified Laplacian are unable  
 324 to accurately represent the intentional change in standoff  
 325 height. The Brenner, Laplacian Energy, and Tenengrad algo-  
 326 rithms all correctly identify optimal standoff height 60%  
 327 into the first layer. This corresponds to the sixth 25.4 mm  
 328 section with the ideal working distance of 12 mm. When  
 329 considering both the time of calculation and the accuracy,  
 330 the Laplacian Energy algorithm was chosen to continue to  
 331 explore in the context of a fabrication. Laplacian Energy  
 332 focus measurement has similarly high accuracy to other  
 333 algorithms evaluated while having the fastest computation  
 334 time, making it suitable for in-situ parameter adjustments.  
 335 Fast computation times are essential for real-time parameter  
 336 adjustments, preventing or minimizing defects like porosity,

overheating, and inconsistent layer bonding. This ensures  
 the production of high-quality components. Due to inconsis-  
 tency in the weld pool, all focus algorithms need focus  
 measurement values from ten images. With a computational  
 time of 3.5 ms per image, the Laplacian Energy algorithm  
 can respond to defects in nearly 35 ms after computing  
 values for all ten images. Further optimizations could be  
 implemented to reduce computation speed and consequently  
 improve machine response time.

### 3.2 Focus measurement in the first layer

After selecting Laplacian Energy as the focus measurement  
 algorithm to continue further exploration with, the first layer  
 was chosen to analyze. The first layer has a known standoff  
 distance and subsequent layers are no longer known with  
 certainty. Results of focus measurement analysis are shown  
 in Fig. 8. The green channel's response is shown, since it  
 coincides with 12 mm standoff height. This was set during

**Fig. 8** Laplacian energy focus measure response for the green channel for each 25.4 mm section

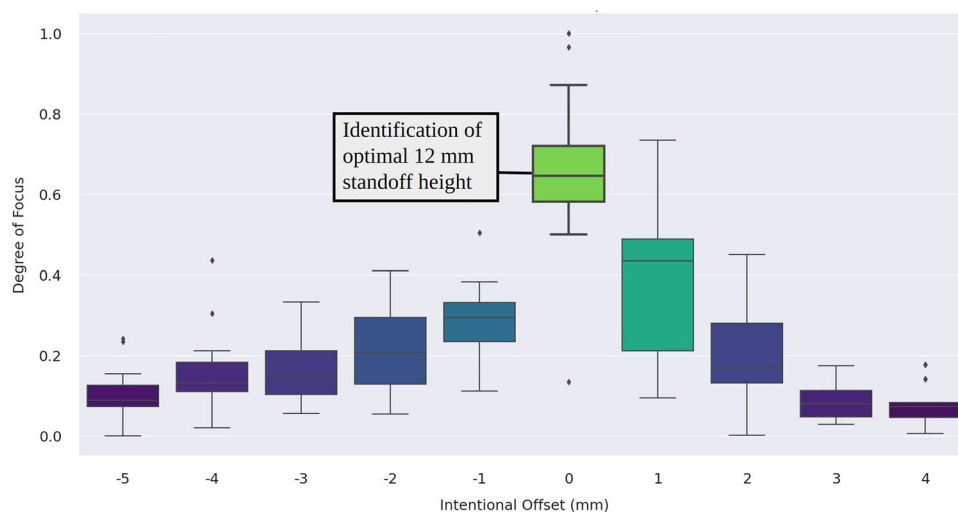
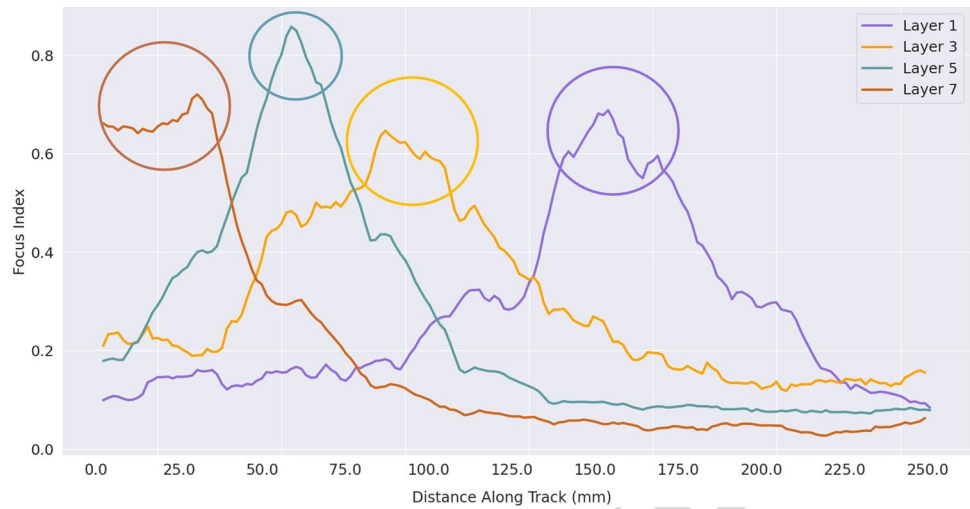


**Fig. 9** Focus measure maximum shifting in subsequent layers due to underbuilding shown through green channel Laplacian energy focus evaluation



354 calibration of the sensor during installation. An optimal  
 355 working distance of 12 mm with an intentional offset of zero  
 356 has a global maximum focus value. Focus evaluation correct-  
 357 ly identifies standoff height.

**3.3 Focus measurement in subsequent layer experiments**

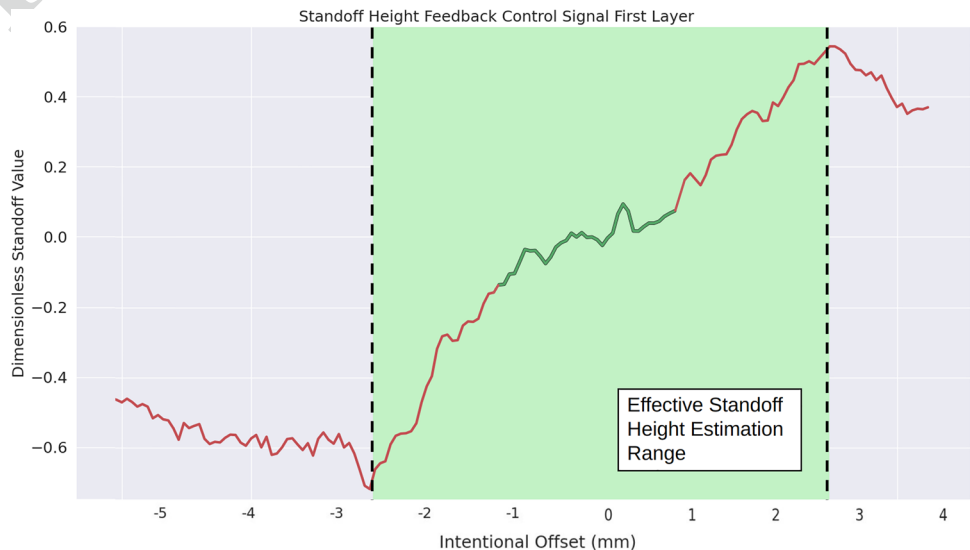
360 Low powder capture on either side of ideal standoff height  
 361 leads to lower deposition height. Successive layers were  
 362 exacerbated by this underbuilding and optimal working  
 363 distance began to move to earlier sections of the wall. In  
 364 Fig. 9, focus measurements for the first four odd layers were  
 365 calculated and plotted. The change in standoff height due to  
 366 overbuilding can be seen as a shift in peak focal index as the  
 367 standoff height is decreasing as more material than intended  
 368 is deposited. Subsequent layers come into focus earlier, indi-  
 369 cating that the standoff height has changed due to reduced

distance between the wall and head. Peak responses for each  
 layer are circled to highlight this change.

**3.4 Focus measurement to generate feedback control signal**

The green band's focal distance lies between red and blue,  
 coinciding with the optimal working distance between the  
 nozzle and weld pool. The control signal was designed with  
 respect to the green band to take advantage of this relation-  
 ship. The focus values from the red and blue channel cancel  
 exactly at the peak focal distance. The red and blue focal  
 responses can be subtracted to form a normalized dimen-  
 sionless signal between  $\pm 1.0$  where zero represents ideal  
 standoff height shown in Fig. 10. The control signal is plot-  
 ted in green at an ideal standoff height of 12 mm with a  
 small tolerance of  $\pm 0.15$  mm. When the feedback control  
 signal is outside this tolerance, the signal is plotted in red

**Fig. 10** Dimensionless standoff-height feedback control signal calculated using Laplacian energy focus evaluation



386 indicating that the current standoff height is no longer at  
 387 an ideal distance. Sensor limitations past standoff height  
 388 of  $\pm 2.5$  mm can no longer distinguish image changes. This  
 389 affects their focus measurement and images captured outside  
 390 of this region are subject to less accurate focus estimation.  
 391 The region within the sensor's ability to accurately estimate  
 392 standoff height is highlighted in light green.

393 **3.5 Reducing focal estimation by counting ejecta**  
 394 **from images**

395 The speed of the printer head and frame rate from the camera  
 396 can be used to identify the number of images captured for  
 397 each 25.4 mm section to create a composite image. There are

18 images per section making 180 images in total for each  
 layer. Extracted weld pools are overlaid consecutively on a  
 larger empty image for each 25.4 mm section, generating ten  
 composite images for each layer—each at different standoff  
 heights. Composite images allow for temporal information  
 to be extracted and identified as features with geographical  
 information included. In addition to high-frequency infor-  
 mation indicating degree of focus, the amount of satellite  
 objects around the melt pool in the form of spatter or uncapt-  
 ured powder decreases as a standoff-height approaches the  
 ideal standoff height and then increases again as the stand-  
 off height continues to diverge from ideal. Figure 11 shows  
 each standoff offset section as a single composite image  
 composed of all corresponding coaxial images during the

Fig. 11 Composite images for each 25.4 mm section in layer 1

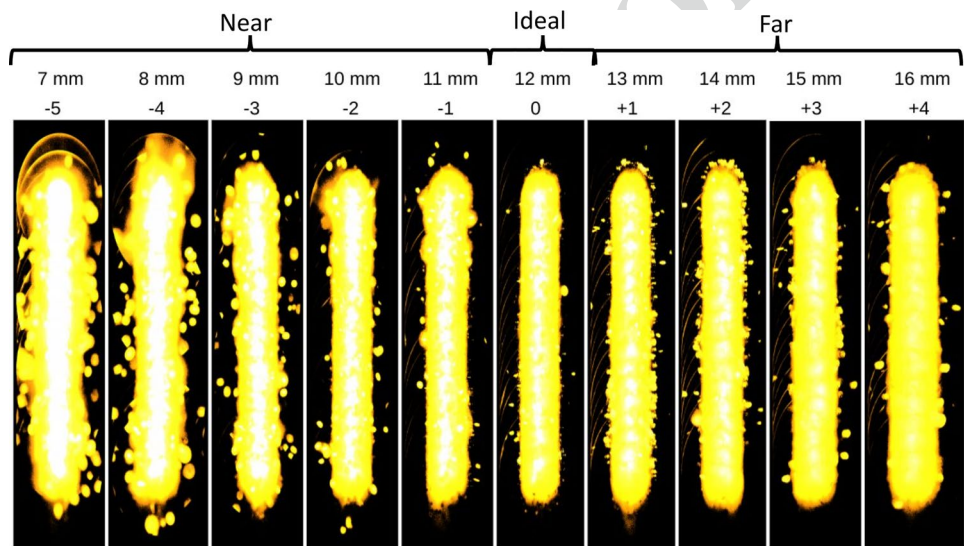
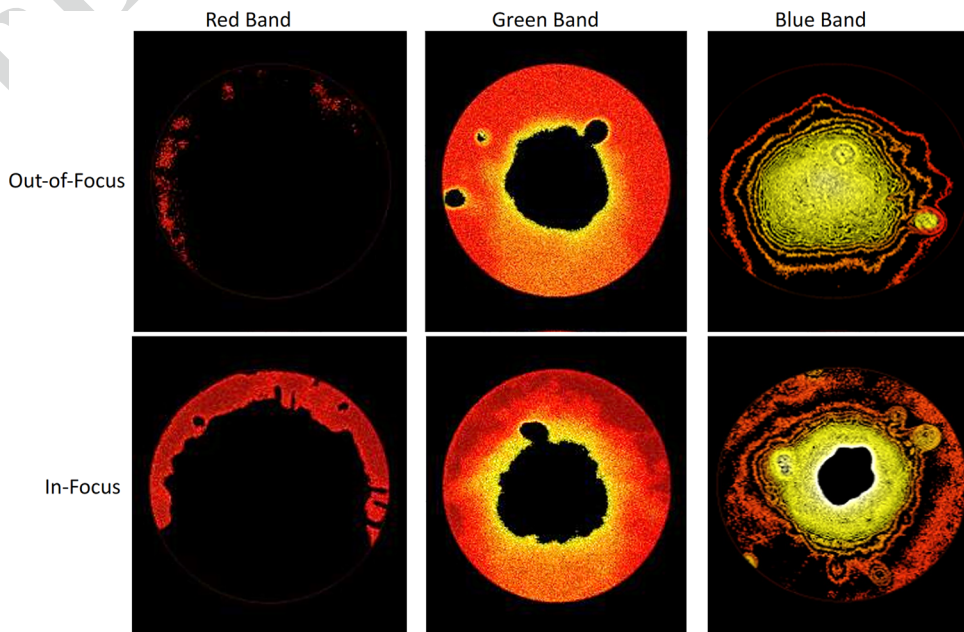


Fig. 12 Comparison of high-frequency information between out-of-focus and in-focus for separate RGB bands found using Laplacian energy kernel



412 deposition of each section. There were ~ 20 images per sec- 434  
 413 tion, each assigned a Cartesian coordinate based on G-Code 435  
 414 and timestamps. 436

415 Due to the increase in ejecta around the weld pool when 437  
 416 the working distance is not in the optimal distance from the 438  
 417 melt pool, ambiguity exists for what the focus algorithm 439  
 418 was detecting in terms of frequency content. More satel- 440  
 419 lite objects in frame would increase the amount of high- 441  
 420 frequency information after feature extraction. Ejecta can 442  
 421 also be in a different plane than the weld pool giving incor- 443  
 422 rect focal information. To identify the main carrier of focal 444  
 423 information, images were split into RGB channels and had 445  
 424 a Laplacian filter operator applied. The resulting images in 446  
 425 Fig. 12 show that the texture of the weld pool accounts for 447  
 426 most of the frequency information and the presence of spat- 448  
 427 ter and uncaptured powder is outweighed by the number of 449  
 428 pixels within the weld pool's frequency information.

### 429 3.6 Ejecta frequency as an alternative method

430 Inspection of the coaxial images yields the fact that the 451  
 431 amount of satellite objects around the weld pool changes 452  
 432 with the intentional standoff-height offset. The objects may 453  
 433 be spatter or potentially uncaptured powder and no attempt 454  
 455  
 456

434 to classify or differentiate between the two is attempted in 435  
 436 this work. The magnitude of ejecta in layer one is plotted 437  
 438 against the focus measurement value in Fig. 13 for compari- 439  
 440 son. Ejecta has more noise with more volatility, so filter- 441  
 442 ing may be required to leverage these process data which 442  
 443 will introduce a phase delay in the output control signal that 443  
 444 could be potentially leveraged. Ejecta is inversely propor- 444  
 445 tional to the standoff height as there is less ejecta with proper 445  
 446 standoff; however, the window of reduced ejecta is narrow 446  
 447 ( $\pm 0.5$  mm versus  $\pm 2.5$  mm for focus) and is therefore less 447  
 448 useful than the focus method. Both extracted features (focus 448  
 449 and spatter) could be simultaneously considered to further 449  
 450 improve the estimation of the optimal working distance.

### 450 3.7 Discussion

451 The presented study explores the application of a three-color 451  
 452 channel focus quantification using a prism-based camera 452  
 453 sensor for real-time standoff-height estimation in Directed 453  
 454 Energy Deposition processes. The focus of both the laser 454  
 455 and powder stream is pivotal for stable and predictable depo- 455  
 456 sition, yet maintaining the precise standoff height is often 456

**Fig. 13** Comparison of Laplacian energy focal measurement and identifying standoff through ejecta

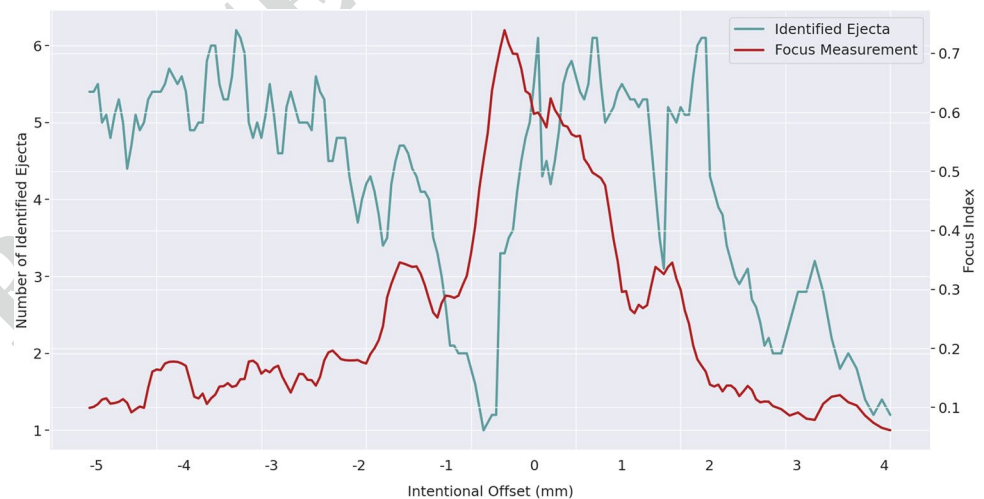


**Table 2** Comparison of alternative standoff measurement methods

Method	Accuracy	Measurement frequency	Cost	Sensitivity to measurement interference	Citations
Color channel focus	~0.5 mm	35 ms	\$ 3500	Sensitive to focus information not associated with weld pool, such as excessive powder particles in image	
Laser displacement sensor	8 $\mu$ m	500 ms	> \$ 5000	Color or surface variations	[50]
Laser triangulation	~ 0.1 mm	30 ms	\$ 3500	Lighting variation, surface roughness, and reflections	[44, 51]
Trinocular optical detector	~ 0.05 mm	100 ms	< \$ 2000	Flashback from other cameras	[42]

457 overlooked in commercial DED systems. While this study  
458 demonstrates effective standoff monitoring, several alter-  
459 native approaches exist commercially and in the literature.  
460 Therefore, a brief comparison of alternatives is presented in  
461 Table 2 and discussed in this section.

462 Laser distance sensors directly measure the distance  
463 between the sensor and the substrate. Structured light  
464 scanning provides detailed 3D surface information  
465 giving high precision and reliability for standoff-height  
466 measurement. However, these methods need specialized  
467 hardware and may struggle with measuring dynamic changes  
468 during the DED process. Alternatively, color channel  
469 focus estimation requires only swapping out coaxial weld  
470 pool cameras, making it simple to adopt into current DED  
471 systems. While effective for in-situ control, the proposed  
472 method may have limitations in achieving high absolute  
473 accuracy.

474 While this study provides insights into real-time  
475 standoff-height estimation in laser-based directed energy  
476 deposition (DED) processes, there are several avenues for  
477 future research and development to further enhance the  
478 applicability and robustness of the proposed approach.  
479 Exploring machine learning techniques to further refine  
480 focus measurement algorithms, especially in the context  
481 of specific material properties and process conditions,  
482 could improve the accuracy of standoff-height estimation.  
483 Integrating in-situ parameter optimization to provide  
484 corrective intervention during deposition. Developing  
485 algorithms that can adjust standoff height in response to  
486 tool path and variations in deposition geometry would be a  
487 valuable extension. Combining standoff-height estimation  
488 with other process parameters, such as laser power,  
489 deposition speed, or material feed rate, could result in a more  
490 comprehensive and adaptive control system. This research  
491 establishes the feasibility of leveraging three-color channel  
492 focus measurements for real-time standoff-height estimation  
493 in laser-based DED processes. The proposed methodology  
494 contributes to enhanced control and adaptability in additive  
495 manufacturing.

## 496 4 Conclusions

497 This effort has demonstrated preliminarily that the  
498 magnitude of focus of three-color channels in a prism-  
499 based camera sensor can be leveraged to estimate the  
500 standoff height of the blown powder laser cladding head.  
501 Monitoring the standoff in real time (less than 5 ms of  
502 computation after receiving a static image) is crucial  
503 to maintain layer thickness and to ensure dimensional  
504 accuracy of the structure being fabricated. With no extra  
505 measurement equipment, the coaxial computer vision focus

506 estimation can provide a reasonable range of 5 mm height  
507 estimation. This system is capable of being used as a control  
508 signal to optimize the processing (e.g.,  $z$  height, deposition  
509 speed, etc.) to improve fabrication. The outcomes of this  
510 research have direct implications for industries relying on  
511 advanced manufacturing, such as aerospace and automotive,  
512 by offering a more adaptable and controlled additive  
513 manufacturing process. Important achievements in this work  
514 include:

- $\pm 2.5$  mm standoff-height estimation range where  
Laplacian energy focus measurement can accurately  
identify standoff height of 12 mm. 515
- The Laplacian energy focus measurement algorithm can  
be applied to an image in 3.5 ms well below the period  
of imaging at 20 frames per second at 50 ms per picture. 516
- Satellite object quantification shows some correlation to  
standoff height but is subject to more volatility. This may  
show improved accuracy when used in conjunction with  
focus evaluation. 517
- Controlling standoff height in real time improves wall  
thickness uniformity. This improves part accuracy and  
production yield. 518

**Acknowledgements** This manuscript has been authored by UT-Bat-  
telle, LLC under Contract No. DE-AC05-00OR22725 with the U.S.  
Department of Energy and University of Texas-El Paso under Con-  
tract No. FA8650-20-2-5700 with Air Force Research Laboratory. This  
effort was performed through the National Center for Defense Manu-  
facturing and Machining under the America Makes Program entitled  
“Hybrid Manufacturing for Rapid Tooling and Repair”. The United  
States Government retains and the publisher, by accepting the article  
for publication, acknowledges that the United States Government  
retains a non-exclusive, paid-up, irrevocable, world-wide license to  
publish or reproduce the published form of this manuscript, or allow  
others to do so, for United States Government purposes. The Depart-  
ment of Energy will provide public access to these results of federally  
sponsored research in accordance with the DOE Public Access Plan  
(<http://energy.gov/downloads/doe-public-access-plan>). The authors  
would like to highlight the support from the Murchison Chair at the  
University of Texas at El Paso. 528

**Disclaimer** The views and conclusions contained in this document  
are those of the authors and should not be interpreted as necessarily  
representing the official policies or endorsements, either expressed or  
implied, of the Air Force Research Laboratory or the U.S. Government. 545

## 549 Declarations

**Conflict of interests** The authors have no competing interests to de-  
clare that are relevant to the content of this article. 550

552 **References**

- 553 1. Dávila JL, Neto PI, Noritomi PY et al (2020) Hybrid manufactur-  
554 ing: a review of the synergy between directed energy deposition  
555 and subtractive processes. *Int J Adv Manuf Technol* 110:3377–  
556 3390. <https://doi.org/10.1007/s00170-020-06062-7>
- 557 2. Lorenz KA, Jones JB, Wimpenny DI, Jackson MR (2015) A  
558 review of hybrid manufacturing. In: Solid freeform fabrica-  
559 tion conference proceedings. [sffsymposium.engr.utexas.edu](http://sffsymposium.engr.utexas.edu), pp  
560 96–108
- 561 3. Zhu Z, Dhokia VG, Nassehi A (2013) A review of hybrid manu-  
562 facturing processes—state of the art and future perspectives.  
563 *Integr Manuf* 26:596–615
- 564 4. Sealy MP, Madireddy G, Williams RE et al (2018) Hybrid pro-  
565 cesses in additive manufacturing. *J Manuf Sci Eng* 140:060801.  
566 <https://doi.org/10.1115/1.4038644>
- 567 5. Gibson I, Rosen D, Stucker B (2015) Directed energy deposi-  
568 tion processes. In: Gibson I, Rosen D, Stucker B (eds) *Additive  
569 manufacturing technologies: 3D printing, rapid prototyping, and  
570 direct digital manufacturing*. Springer, New York, pp 245–268
- 571 6. Manogharan G, Wysk R, Harrysson O, Aman R (2015) AIMS—a  
572 metal additive-hybrid manufacturing system: system architecture  
573 and attributes. *Proc Manuf* 1:273–286
- 574 7. Ahn D-G (2021) Directed energy deposition (DED) process:  
575 state of the art. *Int J Precis Eng Manuf Green Technol* 8:703–  
576 742. <https://doi.org/10.1007/s40684-020-00302-7>
- 577 8. Alammar A, Kois JC, Revilla-León M, Att W (2022) Additive  
578 manufacturing technologies: current status and future perspec-  
579 tives. *J Prosthodont* 31:4–12. <https://doi.org/10.1111/jopr.13477>
- 580 9. Feldhausen T, Heinrich L, Saleeby K et al (2022) Review of  
581 computer-aided manufacturing (CAM) strategies for hybrid  
582 directed energy deposition. *Addit Manuf* 56:102900. <https://doi.org/10.1016/j.addma.2022.102900>
- 583 10. Feenstra DR, Banerjee R, Fraser HL et al (2021) Critical review  
584 of the state of the art in multi-material fabrication via directed  
585 energy deposition. *Curr Opin Solid State Mater Sci* 25:100924.  
586 <https://doi.org/10.1016/j.cossms.2021.100924>
- 587 11. Griffith ML, Harwell LD, Romero JT (1997) Multi-material  
588 processing by LENS. 1997 International
- 589 12. Ambriz S, Coronel J, Zinnel B et al (2017) Material handling  
590 and registration for an additive manufacturing-based hybrid  
591 system. *J Manuf Syst* 45:17–27
- 592 13. Juhasz M, Tiedemann R, Dumstorff G et al (2020) Hybrid  
593 directed energy deposition for fabricating metal structures with  
594 embedded sensors. *Addit Manuf* 35:101397. <https://doi.org/10.1016/j.addma.2020.101397>
- 595 14. Li X, Golnas A, Prinz FB (2000) Shape deposition manufactur-  
596 ing of smart metallic structures with embedded sensors. In:  
597 *Smart structures and materials*
- 598 15. Haley JC, Zheng B, Bertoli US et al (2019) Working distance  
599 passive stability in laser directed energy deposition additive  
600 manufacturing. *Mater Des* 161:86–94. <https://doi.org/10.1016/j.matdes.2018.11.021>
- 601 16. Luo M, Shin YC (2015) Vision-based weld pool boundary  
602 extraction and width measurement during keyhole fiber laser  
603 welding. *Opt Lasers Eng* 64:59–70. <https://doi.org/10.1016/j.optlaseng.2014.07.004>
- 604 17. You D, Gao X, Katayama S (2013) Multiple-optics sensing of  
605 high-brightness disk laser welding process. *NDT E Int* 60:32–39
- 606 18. Gibson BT, Bandari YK, Richardson BS, et al (2019) Melt pool  
607 monitoring for control and data analytics in large-scale metal  
608 additive manufacturing. In: 2019 International
- 609 19. Gibson BT, Bandari YK, Richardson BS et al (2020) Melt  
610 pool size control through multiple closed-loop modalities in  
611 laser-wire directed energy deposition of Ti-6Al-4V. *Addit  
612 Manuf* 32:100993. <https://doi.org/10.1016/j.addma.2019.100993>
- 613 20. Ertay DS, Naiel MA, Vlasea M, Fieguth P (2021) Process per-  
614 formance evaluation and classification via in-situ melt pool  
615 monitoring in directed energy deposition. *CIRP J Manuf Sci  
616 Technol* 35:298–314. <https://doi.org/10.1016/j.cirpj.2021.06.015>
- 617 21. Walker TR, Bennett CJ, Lee TL, Clare AT (2020) A novel numeri-  
618 cal method to predict the transient track geometry and thermo-  
619 mechanical effects through in-situ modification of the process  
620 parameters in Direct Energy Deposition. *Finite Elem Anal Des*  
621 169:103347. <https://doi.org/10.1016/j.finel.2019.103347>
- 622 22. Mondal S, Gwynn D, Ray A, Basak A (2020) Investigation of melt  
623 pool geometry control in additive manufacturing using hybrid  
624 modeling. *Metals* 10:683
- 625 23. Mirkoohi E, Sievers DE, Garmestani H et al (2019) Three-dimen-  
626 sional semi-elliptical modeling of melt pool geometry considering  
627 hatch spacing and time spacing in metal additive manufacturing.  
628 *J Manuf Process* 45:532–543. <https://doi.org/10.1016/j.jmapro.2019.07.028>
- 629 24. Hofman JT, Pathiraj B, van Dijk J et al (2012) A camera-based  
630 feedback control strategy for the laser cladding process. *J Mater  
631 Process Technol* 212:2455–2462
- 632 25. Doubenskaia M, Pavlov M, Grigoriev S, Smurov I (2013) Defini-  
633 tion of brightness temperature and restoration of true tempera-  
634 ture in laser cladding using infrared camera. *Surf Coat Technol*  
635 220:244–247. <https://doi.org/10.1016/j.surfcoat.2012.10.044>
- 636 26. Sampson R, Lancaster R, Sutcliffe M et al (2020) An improved  
637 methodology of melt pool monitoring of direct energy deposi-  
638 tion processes. *Opt Laser Technol* 127:106194. <https://doi.org/10.1016/j.optlastec.2020.106194>
- 639 27. Staudt T, Eschner E, Schmidt M (2019) Temperature determina-  
640 tion in laser welding based upon a hyperspectral imaging tech-  
641 nique. *CIRP Ann Manuf Technol* 68:225–228. <https://doi.org/10.1016/j.cirp.2019.04.117>
- 642 28. Xia C, Pan Z, Li Y et al (2022) Vision-based melt pool monitoring  
643 for wire-arc additive manufacturing using deep learning method.  
644 *Int J Adv Manuf Technol* 120:551–562. <https://doi.org/10.1007/s00170-022-08811-2>
- 645 29. Mi J, Zhang Y, Li H et al (2021) In-situ monitoring laser  
646 based directed energy deposition process with deep convolu-  
647 tional neural network. *J Intell Manuf*. <https://doi.org/10.1007/s10845-021-01820-0>
- 648 30. Esfahani MN, Bappy MM, Bian L, Tian W (2022) In-situ layer-  
649 wise certification for direct laser deposition processes based on  
650 thermal image series analysis. *J Manuf Process* 75:895–902.  
651 <https://doi.org/10.1016/j.jmapro.2021.12.041>
- 652 31. Khanzadeh M, Chowdhury S, Tschopp MA et al (2019) In-situ  
653 monitoring of melt pool images for porosity prediction in directed  
654 energy deposition processes. *IIEE Transactions* 51:437–455.  
655 <https://doi.org/10.1080/24725854.2017.1417656>
- 656 32. Wolff SJ, Wang H, Gould B et al (2021) In situ X-ray imaging of  
657 pore formation mechanisms and dynamics in laser powder-blown  
658 directed energy deposition additive manufacturing. *Int J Mach  
659 Tools Manuf* 166:103743. <https://doi.org/10.1016/j.ijmactools.2021.103743>
- 660 33. Simonds BJ, Tanner J, Artusio-Glimpse A et al (2021) The causal  
661 relationship between melt pool geometry and energy absorption  
662 measured in real time during laser-based manufacturing. *Appl  
663 Mater Today* 23:101049. <https://doi.org/10.1016/j.apmt.2021.101049>
- 664 34. Krotkov E (1988) Focusing. *Int J Comput Vis* 1:223–237
- 665 35. Lee S-Y, Kumar Y, Cho J-M et al (2008) Enhanced autofocus  
666 algorithm using robust focus measure and fuzzy reasoning. *IEEE  
667 Trans Circuits Syst Video Technol* 18:1237–1246

- 680 36. Peddigari V, Gamadia M, Kehtarnavaz N (2005) Real-time imple-  
681 mentation issues in passive automatic focusing for digital still  
682 cameras. [https://library.imaging.org/admin/apis/public/api/ist/  
683 website/downloadArticle/jist/49/2/art00003](https://library.imaging.org/admin/apis/public/api/ist/website/downloadArticle/jist/49/2/art00003). Accessed 11 Mar  
684 2023
- 685 37. Pertuz S, Puig D, Garcia MA (2013) Analysis of focus measure  
686 operators for shape-from-focus. *Pattern Recognit* 46:1415–1432.  
687 <https://doi.org/10.1016/j.patcog.2012.11.011>
- 688 38. Sun Y, Duthaler S, Nelson BJ (2004) Autofocusing in computer  
689 microscopy: selecting the optimal focus algorithm. *Microsc Res*  
690 *Tech* 65:139–149. <https://doi.org/10.1002/jemt.20118>
- 691 39. Herrmann C, Bowen RS, Wadhwa N, et al (2020) Learning to  
692 Autofocus. 2020 IEEE/CVF Conference on Computer Vision and  
693 Pattern Recognition (CVPR)
- 694 40. Wang D, Song C, Yang Y, Bai Y (2016) Investigation of crystal  
695 growth mechanism during selective laser melting and mechanical  
696 property characterization of 316L stainless steel parts. *Mater Des*  
697 100:291–299. <https://doi.org/10.1016/j.matdes.2016.03.111>
- 698 41. Kono D, Yamaguchi H, Oda Y, Sakai T (2020) Stabilization of  
699 standoff distance by efficient and adaptive updating of layer height  
700 command in directed energy deposition. *CIRP J Manuf Sci Technol*  
701 31:244–250. <https://doi.org/10.1016/j.cirpj.2020.05.015>
- 702 42. Asselin M, Toyserkani E, Irvani-Tabrizipour M, Khajepour A  
703 (2005) Development of trinocular CCD-based optical detector  
704 for real-time monitoring of laser cladding. In: *IEEE International  
705 Conference Mechatronics and Automation*
- 706 43. Irvani-Tabrizipour M, Toyserkani E (2007) An image-based  
707 feature tracking algorithm for real-time measurement of clad  
708 height. *Mach Vis Appl* 18:343–354. [https://doi.org/10.1007/  
709 s00138-006-0066-7](https://doi.org/10.1007/s00138-006-0066-7)
- 710 44. Borovkov H, de la Yedra AG, Zurutuza X et al (2021) In-line  
711 height measurement technique for directed energy deposition pro-  
712 cesses. *J Mater Process Manuf Sci* 5:85. [https://doi.org/10.3390/  
713 jmmp5030085](https://doi.org/10.3390/jmmp5030085)
- 714 45. Song L, Bagavath-Singh V, Dutta B, Mazumder J (2012) Control  
715 of melt pool temperature and deposition height during direct metal  
716 deposition process. *Int J Adv Manuf Technol* 58:247–256. [https://  
717 doi.org/10.1007/s00170-011-3395-2](https://doi.org/10.1007/s00170-011-3395-2)
- 718 46. Biegler M, Graf B, Rethmeier M (2018) In-situ distortions in  
719 LMD additive manufacturing walls can be measured with digi-  
720 tal image correlation and predicted using numerical simulations.  
721 *Addit Manuf* 20:101–110. [https://doi.org/10.1016/j.addma.2017.  
722 12.007](https://doi.org/10.1016/j.addma.2017.12.007)
- 723 47. Garmendia I, Pujana J, Lamikiz A et al (2019) Structured light-  
724 based height control for laser metal deposition. *J Manuf Process*  
725 42:20–27. <https://doi.org/10.1016/j.jmapro.2019.04.018>
- 726 48. Heralić A, Christiansson A-K, Lennartson B (2012) Height con-  
727 trol of laser metal-wire deposition based on iterative learning con-  
728 trol and 3D scanning. *Opt Lasers Eng* 50:1230–1241. [https://doi.  
729 org/10.1016/j.optlaseng.2012.03.016](https://doi.org/10.1016/j.optlaseng.2012.03.016)
- 730 49. Heigel JC, Michaleris P, Palmer TA (2015) In situ monitoring and  
731 characterization of distortion during laser cladding of Inconel@  
732 625. *J Mater Process Technol* 220:135–145
- 733 50. Tang L, Ruan J, Sparks TE et al (2009) Layer-to-layer height  
734 control of laser metal deposition processes. In: *2009 American  
735 Control Conference*
- 736 51. Donadello S, Motta M, Demir AG, Previtali B (2019) Monitoring  
737 of laser metal deposition height by means of coaxial laser trian-  
738 gulation. *Opt Lasers Eng* 112:136–144. [https://doi.org/10.1016/j.  
739 optlaseng.2018.09.012](https://doi.org/10.1016/j.optlaseng.2018.09.012)
- 740 52. Hand DP, Fox MDT, Haran FM et al (2000) Optical focus con-  
741 trol system for laser welding and direct casting. *Opt Lasers Eng*  
742 34:415–427
- 743 53. Alexander Z, DeVol N, Emig M et al (2022) Support vector  
744 machines for classification of direct energy deposition stand-  
745 off distance for improved process control. Volume 1: *Additive  
746 Manufacturing; Biomanufacturing; Life Cycle Engineering;  
747 Manufacturing Equipment and Automation; Nano/Micro/Meso  
748 Manufacturing*
- 749 **Publisher's Note** Springer Nature remains neutral with regard to  
750 jurisdictional claims in published maps and institutional affiliations.  
751
- 752 Springer Nature or its licensor (e.g. a society or other partner) holds  
753 exclusive rights to this article under a publishing agreement with the  
754 author(s) or other rightsholder(s); author self-archiving of the accepted  
755 manuscript version of this article is solely governed by the terms of  
756 such publishing agreement and applicable law.  
757  
758